

A ubiquitous transfer function links interacting elements to emerging property of complex systems

Authors: Lina Yan^{1†}, Jeffrey Huy Khong^{2†}, Aleksandar Kostadinov³, Jerry Ying Hsi Fuh^{1*}, Chih-Ming Ho^{1,4*}

Affiliations:

¹Department of Mechanical Engineering, National University of Singapore; Singapore, 119077, Singapore.

²Department of Psychology, University of California, Los Angeles; Los Angeles, 90095, United States of America.

³Department of Biological Sciences, National University of Singapore; Singapore, 119077, Singapore.

⁴ Department of Mechanical and Aerospace Engineering, University of California, Los Angeles; Los Angeles, 90095, United States of America.

*Corresponding author. Email: c.ho1945@gmail.com

†These authors contributed equally to this work.

Abstract: In the field of complex systems, self-organization magnifies the compounding effects of element interactions by propagating, modifying, and enhancing functionality, ultimately leading to emergent system properties. The intricacies of self-organization make unveiling the elusive link between element interactions and emergent system properties akin to finding the proverbial Holy Grail. In the search for identifying a method to predict system-level properties, we used an inductive approach to bypass the self-organization. By observing drug interactions within biological complex system, system property, efficacy, emerged as a smooth response surface in the multi-dimensional space of drug-system interactions, which can be represented by the Complex System Response (CSR) function. This CSR function has been successfully validated across diverse disease models in cell lines, animals, and clinical trials. Notably, the CSR function reveals that biological complex systems exhibit second-order non-linearity. In this study, we generalized the CSR function to physical complex systems, linking maximum compressive yielding stress to impactful manufacturing parameters of the Selective Laser Melting (SLM) process. Remarkably though anticipated, the CSR function reveals the connection between the macroscale system property (compressive yielding stress) and the microstructure during self-organizing process. In addition, the second-order non-linear CSR functions ensure a single global optimum in complex systems.

A Transfer Function Linking Constituent Elements to Emerging System Properties

The field of complex systems (1–8) is an emerging branch of physics. In this study, we adopted the following definition (9) for the studies of complex systems.

1. A complex system comprises a large number of interacting elements.
2. The effects of interactions propagate and connect elements, self-organizing them into a nonlinear dynamic complex system.
3. The emergent properties of a complex system are challenging to trace back to the interacting elements due to the intricate self-organizing processes.
4. A complex system is usually adaptive and robust.

In biological, physical, chemical and social complex systems, establishing a quantitative relationship between emergent properties (such as health conditions, physical and chemical material properties, or economic indices) and their respective elements (such as therapeutic agents, manufacturing parameters, or monetary policies) is critical for understanding the fundamentals of complex systems and to facilitate their manipulation and application.

In the case of biological complex systems, the intricate interactions among drugs and cellular elements propagate through cellular networks. This signaling cascades through higher-level systems such as tissues, organs, and the entire body. At each stage, the self-organization of interacting elements within these subsystems differs from the previous stage, yet each possesses multifaceted functionalities. This information dissemination and process reorganization are non-deterministic and, thus, lack unified rules. As a result, the reductive methodology (10–13) encounters significant impediments in addressing self-organization, thereby rendering the establishment of relationships between interacting elements and emergent properties exceedingly arduous; current studies of complex systems often rely on model-based equations (14–19) or network analysis (20–22) (additional information provided in Supplementary materials, Text section 1).

Complex Systems Response (CSR) Function for Biological Complex Systems

In a diseased body, drugs interact with disease-causing agents and physiological mechanisms to combat the illness. Achieving improved system outcomes necessitates a qualitative transfer function that links a specific drug-dose stimulation to systemic efficacy. Contrary to making use of reductive methods to identify systemic outcomes based on element interactions, we chose to employ inductive reasoning, which can bypass the analysis of intricate self-organization and is, therefore, a mechanism-free approach. This inductive approach involves four steps: 1) observing natural phenomenon, 2) directly uncovering system response patterns, 3) formatting the discovery, and 4) generalizing the discovery.

In our prior study, based on experimental evidence of ATP production in a cancer cell line stimulated by a combinatorial regimen (23), artificial neural networks were employed as a method for inductive reasoning (Supplementary Materials, Text section 2). The emergent property, the expression level of ATP level, was uncovered to be a smooth multi-dimensional surface in relation to the drug-dose variations. Through regression analysis, this surface, which may exhibit an elliptic paraboloid or a hyperbolic paraboloid shape, is represented by a second-order nonlinear Complex Systems Response (CSR) function (Function-1).

$$E(c_i, u_x, t) = x_0(u_x, t) + \sum_{\substack{i=1 \\ k \neq i}}^P x_i(c_k, u_x, t) c_i(t) + \sum_{\substack{i=1 \\ k \neq i}}^P x_{ii}(c_k, u_x, t) c_i^2(t) + \sum_{\substack{i=1 \\ k \neq i \\ \text{and} \\ k \neq j}}^{P-1} \sum_{j=i+1}^P x_{ij}(c_k, u_x, t) c_i(t) c_j(t)$$

.....(Function-1)

Where, $E(c_i, u_x, t)$ represents the efficacy or the system response, where $c_i(t)$ denotes the dose level of drug i , serving as controllable parameters, and u_x represents unknown parameters. The coefficient $x_i(c_k, u_x, t)$ signifies the cell response to $c_i(t)$, while $c_i^2(t)$ represents the second order term of $c_i(t)$. Additionally, $x_{ii}(c_k, u_x, t)$ represents the cell response to $c_i^2(t)$, while $x_{ij}(c_k, u_x, t)$ characterize the cell response to the drug-drug interactions between $c_i(t)$ and $c_j(t)$.

Following the above-described steps of observation and pattern identification for establishing the discovery of the CSR function, Function-1, has been generalized and verified across a diverse range of disease models, including cellular (23–30), animal (31–33), and clinical trials (34–37). In Function-1, the terms on the right side represent the drug molecules interacting with complex systems, while the term on the left side denotes the emergent property of the system resulting from drug stimulations, i.e., system efficacy. The CSR function exhibits second-order non-linearity, a fundamental characteristic of complex systems. This second-order non-linear nature of Function-1 implies that the system response $E(c_i, u_x, t)$ has a single global optimum, a versatile finding for the application of complex systems. Moreover, the CSR function illustrates drug-drug interactions, delineating drug synergisms or antagonisms that vary over time and among individual patients. These findings lead to the realization that, contrary to common belief, synergism and antagonism are not inherent properties of drugs but are, in fact, dynamic properties influenced by multiple factors (32).

In current cancer therapeutics, dosage determinations are based on population-averaged values. However, there is a significant diversity among cancer patients (38), which is why chemotherapy often results in less satisfactory efficacies (39). Hence, our interest lies in the development of personalized medicine (36–39) which customizes combinatorial treatment for individual patients based on phenotypic outcomes rather than genomic information (40). However, the appeal of crafting a customized treatment for each patient is, hampered by an insurmountable practical limitation: with L dosing levels for each drug among a pool of P drugs, the resulting L^P drug-dose combinations create a large search space that is impractical to exhaustively explore. The Function-1 comprises $(P^2 + 3P + 2) / 2$ coefficients, by conducting a small number $(P^2 + 3P + 2) / 2 \ll L^P$ of calibration tests on a specific patient's body system, instead of relying on the data collected from a population of patients and using big-data deep learning approaches. In contrary, the here-suggested method requires a comparatively miniscule amount of data: after having obtained a small number of calibration tests of one patient, the personalized-response coefficients of the CSR function can then be determined by a straightforward protocol (Supplementary Materials, Text section 2.3). This approach allows us to find the maximum efficacy and the corresponding optimal personalized drug-dose combinations for an individual patient in clinical trials including medication for cancer, organ transplant, HIV and cognitive training (36–39). Significant improvements of the therapeutic outcomes were observed across all these personalized clinical trials.

CSR Function for Physical Complex Systems

As with biological complex systems, the ability to predict the emergent properties of physical complex systems is of equal interest. Given that the CSR function relies on mechanism-free inductive reasoning, it stands to reason that it could be applicable to other complex systems as well. In this study, our primary goal is to explore whether the CSR function can be generalized to physical complex systems.

Selective Laser Melting (SLM) was chosen for this study due to its interesting self-organization process and its relevance and unprecedented potential in the manufacturing industry. However, it struggles from a high order of process parameters which renders the process as a valuable example for a physical complex system allowing us to test CSR method. SLM uses a high-energy laser beam to melt particles at a specific area within a bed of metal powders. As the laser acts upon the powders, it creates a melt pool that subsequently cools and solidifies. The designed laser scanning path can produce precise and intricate structures. The compressive or tensile yielding stress is among the emergent material properties (41–44).

During the solidification, metal atoms self-organize into hierarchical complex systems, forming crystalline lattices and grains accompanied by dislocations and precipitates until the liquid metal solidifies (45–47). This self-organization process heavily depends on the interactions between manufacturing parameter-level combinations and metal powders. In addition to validating the applicability of the CSR function in physical complex systems, self-organization process of physical complex systems is simpler than biological complex systems and may offer opportunities to understand how variations in self-organization relate to emergent system properties.

While there are dozens of processing parameters in SLM, our study focuses solely on three parameters that strongly influence on the melting and solidification process, namely laser power (P), scanning velocity (V), and powder bed temperature (T) (Supplementary Materials, Text section 3). The energy density, $E = P / (V \times h \times l)$, is the amount of laser energy delivered per unit area, where h is the default hatch distance (0.08 mm), and l is the layer thickness of the powder for each print path (0.02 mm). The energy density determines the shape and size of melt pool in the melting process (Supplementary Materials test section 3.4). The temperature (T) scales to the global temperature gradient between the melting pool and the environment, determining the rate of heat removal from the melt pool during the solidification. In our study, P , V , and T , were chosen as the manufacturing parameters (Function-2), while E and T were used as parameters for analyzing the experimental data (Function-3). This approach aims to elucidate how these critical parameters affect the self-organization process and the resulting emergent material properties.

$$\begin{aligned} \text{CYS}(P, V, T, u_x) &= x_0(u_x) + x_p(V, T, u_x) \times P + x_v(P, T, u_x) \times V + x_T(V, P, u_x) \times T \\ &+ x_{pp}(V, T, u_x) \times P^2 + x_{vv}(P, T, u_x) \times V^2 + x_{TT}(V, P, u_x) \times T^2 \\ &+ x_{pV}(T, u_x) \times P \times V + x_{pT}(V, u_x) \times P \times T + x_{VT}(P, u_x) \times V \times T \\ &\dots\dots(\text{Function-2}) \end{aligned}$$

$$\begin{aligned} \text{CYS}(E, T, u_x) &= x_0(u_x) + x_E(T, u_x) \times E + x_T(E, u_x) \times T + x_{EE}(T, u_x) \times E^2 + x_{TT}(E, u_x) \times T^2 \\ &+ x_{ET}(u_x) \times E \times T \\ &\dots\dots(\text{Function-3}) \end{aligned}$$

For three process parameters, P , V , and T , a minimum of ten specimens (Supplementary Materials, Text section 3) is required to solve the coefficients of Function-2. The specimens manufacturing, however, some combinations of P , V , and T may produce distorted specimens due to overheating or result in porous specimens due to underheating, which are not known a priori. Hence, 60 % more specimens were printed than the required number of coefficients to compensate for the potentially flawed print results that would not qualify for the mechanical tests. Of the 16 printed specimens, 5 were aborted (see details in Supplementary Materials, Table S1). The process parameters and the remaining 11 specimens were used to determine the compressive yield stress (Table S1). The CSR function with the two manufacturing parameters, E and T (Supplementary Materials, Table S2) is,

$$\begin{aligned}
 CYS = & -7.54 \times 10 + 1.12 \times 10 \times E + 7.94 \times 10^{-1} \times T - 5.55 \times 10^{-2} \times E^2 - 3.59 \times 10^{-3} \times T^2 \\
 & + 7.38 \times 10^{-4} \times E \times T \\
 & \dots\dots(\text{Function-4})
 \end{aligned}$$

The CSR surface, shown in Fig. 1, exhibits a concave elliptic paraboloid geometry. The high R^2 value of 0.898 validated that the data satisfied the CSR function in SLM manufacturing. The response surface provides an overview of the compressive yield stress (CYS) and its variation with the levels of parameters, E and T , in a multidimensional landscape. The global maximum $CYS = 545$ MPa, which occurred at $E = 102$ J/mm³ and $T = 121^\circ\text{C}$ (Supplementary Materials, Table S3). The maximum CYS determined from the 11 specimens from the CSR functions agreed with the reported CYS measured by trial-and-error method, which required significantly more specimens and tests (Supplementary Materials, Table S4).

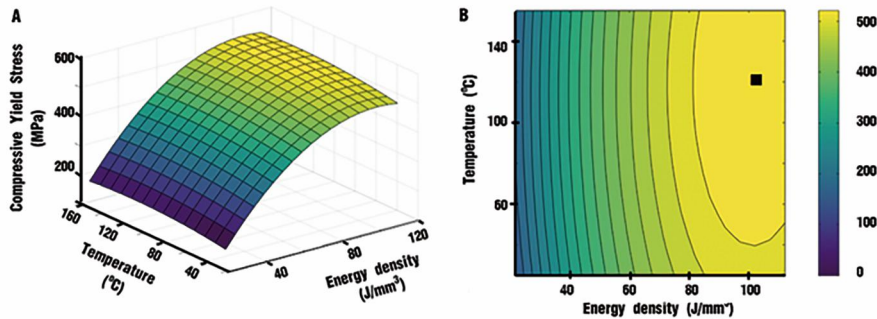


Fig. 1. CSR surface as a function of E and T .

(A). The surface plot of CYS as a function of E and T , the R square of fitting is 0.898.

(B). The contour plot of CYS as a function of E and T , the black dot indicates the maximum CYS at 545 MPa when E at 102 J/mm³ and T at 121 $^\circ\text{C}$.

Searching for extrema in multidimensional spaces is an active area of research in applied sciences, garnering significant interest in fields such as the Monte Carlo method and deep learning with neural networks trained on big data. Typically, databases for these methods are constructed from multiple complex systems, leading to numerous local maxima and minima. The CSR function stands out by being uniquely based on a single complex system and characterized by second-order non-linearity, resulting in the presence of only one global extremum. In addition, only $(P^2 + 3P + 2) / 2$ calibration tests, rather than L^P tests, are

required for our method. These attributes of the CSR function have made the seemingly impossible personalized medicine in biological complex systems achievable. In physical complex systems, this novel function can lead to new frontiers, such as dynamically optimizing the level of each parameter during the manufacturing process, potentially resulting in unexpected material properties, offering significant advancements in the field.

Self-Organization of Physical Complex Systems

In physical complex systems, the mechanisms of self-organization are comparatively less convoluted than biological complex systems: during the phase transition of solidification, thermally excited metal atoms self-organize into crystalline lattices, grains, then hierarchical complex microstructures until the liquid metal solidifies (45–47). While the mechanism description provides insight into the natural phenomenon, it does not offer quantitative information. The mechanism-free CSR surface (Figure 1), on the other hand, provides a quantitative map of how the system response, *CYS*, varies across the multidimensional parameter space. Combining microscale self-organization mechanisms with the macroscale CSR map allows for a comprehensive understanding of physical complex systems.

The CSR function (Function-3) includes the $x_o(u_x, t)$ term, the sum of linear terms, the sum of the second-order terms, and the sum of the interaction terms. The pie charts illustrating the results of the various SLM tests for optimal and off-optimal *CYS* are shown in Fig. 2 (Supplementary Materials, Table S5). From this figure, it is evident that the $x_o(u_x, t)$ term and the interaction term are negligible (Function-5). Thus, only 2P specimens, instead of $(P^2+3P+2)/2$ specimens, need to be printed to determine the coefficients of Function-5. The temperature terms are smaller compared to the energy density terms in both the linear and second-order terms. Subsequently, Function-5 can be approximated to Function-6. The powder bed temperature ranged from 25°C to 160°C which is significantly lower than the melting temperature of SS316L, which lies at 1400°C. As a consequence, the terms involving temperature are negligible. The second-order term of energy density (*E*) has a minor negative value, simplifying Function-6 to Function-7. Consequently, the study of self-organization in this case can approximately rely on variations in energy density alone.

$$CYS(E, T) = x_E(T, u_x) \times E + x_T(E, u_x) \times T + x_{EE}(T, u_x) \times E^2 + x_{TT}(E, u_x) \times T^2$$

..... (Function-5)

$$CYS(E, T) = x_E(T, u_x) \times E + x_{EE}(T, u_x) \times E^2$$

.....(Function-6)

$$CYS(E, T) = x_E(T, u_x) \times E$$

.....(Function-7)

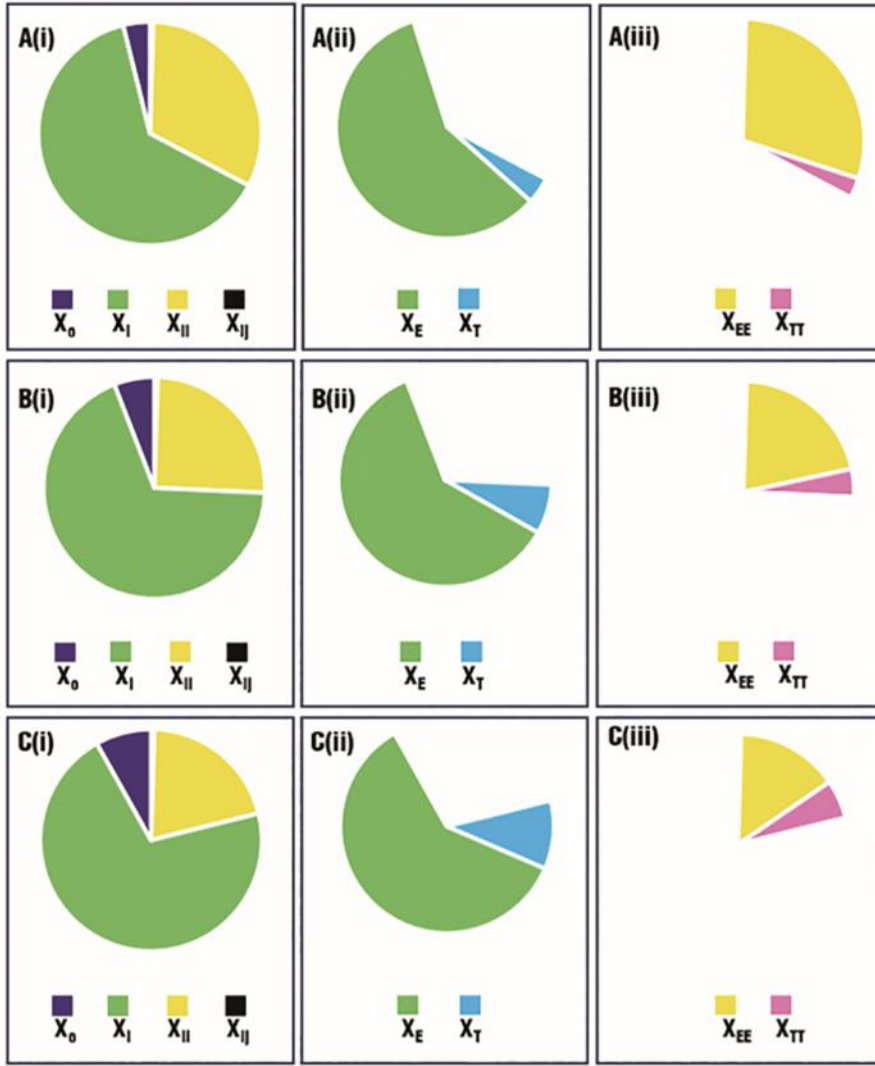


Fig. 2: The Pi chart of the contribution terms to optimal CYS (A) and off-optimal CYS (B and C).

The Pie chart is plotted using equation: $[|X_0| + |X_i| + |X_{ii}| + |X_{ij}|] / CYS_{abs} = 1$

Where,

$$[|X_0| + |X_i| + |X_{ii}| + |X_{ij}|] = CYS_{abs}$$

$$X_0 = x_0(u_x) / CYS_{abs}$$

$$X_i = [X_E + X_T] / CYS_{abs} = [x_E(T, u_x) \times E] / CYS_{abs} + [x_T(E, u_x) \times T] / CYS_{abs}$$

$$X_{ii} = [X_{EE} + X_{TT}] / CYS_{abs} = [x_{EE}(T, u_x) \times E^2] / CYS_{abs} + [x_{TT}(E, u_x) \times T^2] / CYS_{abs}$$

$$X_{ij} = X_{ET} / CYS_{abs} = x_{ET}(u_x) \times E \times T / CYS_{abs}$$

The pie charts for three different energy density levels at the same powder bed temperature, $T=121^\circ\text{C}$, are plotted here.

A(i): When $E = 102 \text{ J/mm}^3$, $T = 121^\circ\text{C}$, the $CYS = 545 \text{ MPa}$, the X_0 , X_i , X_{ii} , and X_{ij} contributed 3.9%, 63.4%, -32.3% and 0.5%, respectively; A(ii): for the term X_i , X_E and X_T contributed 58.5% and 4.9%; A(iii): for the term X_{ii} , X_{EE} and X_{TT} contributed -29.6% and -2.7%.

B(i): When $E = 70 \text{ J/mm}^3$, $T = 121^\circ\text{C}$, $CYS = 488.34 \text{ MPa}$, the X_0 , X_i , X_{ii} , and X_{ij} contributed 5.9%, 68.4%, -25.2% and 0.5%; B(ii): for the term X_i , X_E and X_T contributed 61% and 7.4%; B(iii): for the term X_{ii} , X_{EE} and X_{TT} contributed -21.1% and -4.1%.

C(i): When $E = 50 \text{ J/mm}^3$, $T = 121^\circ\text{C}$, $CYS = 395.21 \text{ MPa}$, the values of X_0 , X_i , X_{ii} , and X_{ij} contributed 8.1%, 70.8%, -20.6% and 0.5%, respectively; C(ii) for the term X_i , X_E and X_T contributed 60.4% and 10.4%; C(iii): for the term X_{ii} , X_{EE} and X_{TT} contributed -15% and -5.6%.

Figure 3-A shows the laser power that was provided to create the tested melt pool, P/VMP , as a function of the E . Around $E = 33.3 \text{ J/mm}^3$, the value of P/VMP is about 45 J/mm^3 . The width (W) and depth (D) of the melt pool, normalized to the laser beam diameter ($d = 0.08 \text{ mm}$) and layer thickness ($l = 0.02 \text{ mm}$), were $W/d = 0.83$ and $D/l = 1.2$, respectively. At $E = 33.3 \text{ J/mm}^3$, the values of W/d and D/l both approximately 20% lower than the average values of 1.03 and 1.59 when tested in the range of $E = 50\text{-}110 \text{ J/mm}^3$ (Figures 3-B and 3-C). The smaller normalized W and D indicate smaller melt pool formed under the corresponding parameter-level combination. In addition, the volumetric area fraction of density ($VAFD$) (Supplementary Materials, Section 3.3 and Table S-6), which represents the ratio of solidified volume to the total volume, was at 60% (Figure 3-D). The low value of laser power spent on melting indicated that most of the heat was dissipated to the surroundings, leaving insufficient heat for melting, which results in low values of W/d , D/l and $VAFD$.

At $E = 47.6 \text{ J/mm}^3$, two specimens were printed at 25°C and 160°C , the P/VMP were decreased to 34.8 and 41.7 J/mm^3 (Figure 3-A). However, the W/d increased to 1.0 and 1.1, while D/l increased to 1.6 and 1.8, respectively. This indicates the melt pool width approached to the laser spot size, and the depth has penetrated to the previously solidified layer. The input laser power has been used to melt the previous layer, therefore decreased the porosity. The $VAFD$ increased from 60% at $E = 33.3 \text{ J/mm}^3$ to 85% at $E = 47.6 \text{ J/mm}^3$.

For $E > 83.3 \text{ J/mm}^3$, the W/d and D/l kept above the average of 1.03 and 1.59, and the $VAFD$ reached 100%. At high values of E , e.g., $E = 222.2 \text{ J/mm}^3$ (S1-11) and $E = 263.9 \text{ J/mm}^3$ (S1-3) (Supplementary Materials, Table S-1), the laser power applied at the print site is higher than the heat transfer rate would allow. This results in overheat which deforms the shape of the specimen and reduce the yield stress.

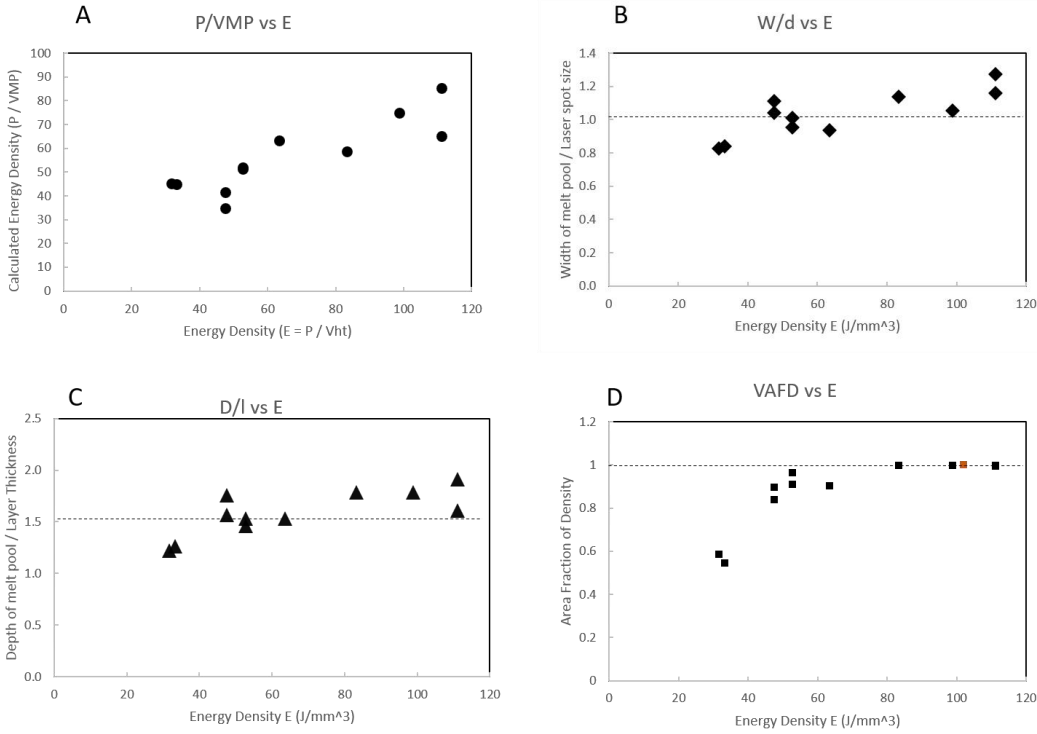


Fig. 3: The variations of volume of melt pool (VMP) and volumetric area fraction of density ($VAFD$) as a function of the energy density (E). The brown dot is the data derived from the maximum CYS predicted by Function-1 at $E = 102 J/mm^3$ and $T = 121^\circ C$.

(A) The laser power input distributed on the volumetric melt pool, VMP , as a function of the energy density, E .

(B) The width of melt pool boundary, W , normalized to the diameter of laser beam, d , as a function of the energy density, E .

(C) The depth of melt pool boundary, D , normalized to the layer thickness, l , as a function of the energy density, E .

(D) The volumetric area fraction of density, $VAFD$, as a function of the energy density, E .

The Maximum CYS of the SLM-fabricated SS316L specimen reported in our study is 545 MPa which is approximately twice that of water-quenched cast SS316, which is 250-290 MPa (48). This disparity arises from the different cooling rates. While the cooling rate of water-quenched cast iron is about $1,000^\circ C/sec$, in here-utilized fabrication method, a laser beam with a scanning speed of 500-2,000 mm/sec moves through a laser spot with a diameter of 0.08 mm which results in solidification time constants ranging from 50-200 μ -sec (Figure 4-A). Given the melting temperature of SS316L, $1400^\circ C$, the cooling rate is in the order of $10^6^\circ C/sec$, which is in the reported range (49). High cooling rates produce more nuclei during solidification, significantly reducing the time available for atoms to diffuse and form larger grains. This rapid cooling leads to the formation of a large number of small nuclei almost simultaneously, resulting in a finer grain size. The finer microstructure provides more grain boundary area, which impedes dislocation movement and increases the CYS (50). The phase transition, melt-solidification, time in this study has very short time scale, 50-200 μ -sec (Figure 4-A). Real-time multiscale analysis

combining physics-based modeling and real-time experimental studies (51-53) will be necessary to uncover the underlying microstructure-property relationships and provide insights into the dynamic phase transition process.

At E in the range of 33.3 J/mm^3 , the CYS is 250 MPa , as shown in Figure 4-B. This relatively low CYS is attributed to near 40% of the specimen volume remaining not melted. As E increases, P/VMP reached a minimal at $E = 47.6 \text{ J/mm}^3$ (Figure 3-A). Thereafter, both CYS (Figure 4-B) and the $VAFD$ (Figure 4-C) see a significant rise from $E = 47.6 \text{ J/mm}^3$ to $E = 83.3 \text{ J/mm}^3$, the CYS continues to increase, albeit at a slower rate. The ratio of CYS to $VAFD$ (Figure 4-C) in the range from $E=33.3 \text{ J/mm}^3$ to $E=83.3 \text{ J/mm}^3$ represents the yield stress contributed by the solidified portion of the specimen. For $E < 83.3 \text{ J/mm}^3$, the average value of $CYS/VAFD$ is 462 MPa , with an averaged time constant of $50 \mu\text{s}$. Beyond $E = 83.3 \text{ J/mm}^3$, CYS , reaching a maximum of 545 MPa at $E = 105 \text{ J/mm}^3$. The averaged CYS between $E = 83.3$ and 111.1 J/mm^3 is 524 MPa and the time constant varied from $100\text{-}200 \mu\text{-sec}$. As E further increases, i.e., $E=222.2 \text{ J/mm}^3$ (S1-11), the laser power provided at the print site is more than the heat transfer rate can remove, overheating will take place and will distort the shape of the specimen and reduce the yield stress.

Metal atoms self-organize into crystalline lattices, forming grains whose boundaries resist dislocation motion and contribute to the material's yield stress. However, most of the laser energy dissipated through global heat transfer, ranging from 33.3 to 83.3 J/mm^3 , is insufficient to self-organize all the metal atoms into grains, resulting in porous specimens with low CYS . The maximum yield stress is achieved by striking a balance between the energy needed for self-organization and the heat removal. A homogeneous complex system forms as volumetric AFD reaches 1. If the real-time analyses (51–53) can establish a quantitative mechanistic relationship of phase change, from melting to self-organization, a reductive approach may link metal atomic level organization to their mechanical properties. The CSR function can quantitatively elucidate self-organization at the microscale and heat removal at the global scale. Additionally, it can guide the optimization of parameters and their levels to achieve a delicate balance, maximizing yield stress.

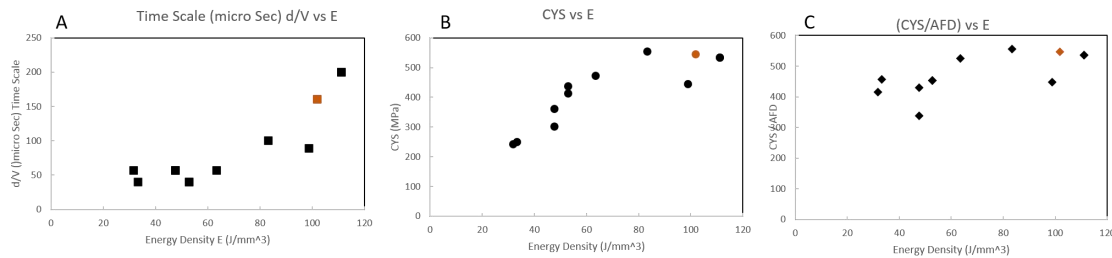


Figure 4: Variations of Melt-solidification time scale and compressive yield stress as a function of the energy density. The brown dot is the data derived from the maximum CYS predicted by Function-1 at $E = 102 \text{ J/mm}^3$ and $T = 121^\circ\text{C}$. The S1-15 ($E = 98.8 \text{ J/mm}^3$) is not an outlier, it was printed at the powder bed temperature of 25°C , which was much lower than 121°C for maximum CYS .

- A: Time scale, d/V , varies with energy density. The d is the diameter of laser beam and V is the laser speed.
- B: Variations of compressive yield stress as a function of energy density.
- C: Estimated CYS of the solidified portion varies as a function of energy density.

Conclusion

In this study, the CSR function, originally discovered in biological complex systems, has been successfully generalized to physical complex systems. The CSR function quantitatively links interacting elements undergoing self-organization to emergent properties. These complex systems exhibit second-order nonlinearity, inherently leading to a global extremum. In the context of physical complex systems, the CSR function can elucidate the relationship between the macroscale system property, *CYS*, and the self-organization characteristics of the microstructure at the atomic scale.

Acknowledgments:

We extend our gratitude to the National University of Singapore Centre for Additive Manufacturing for providing the fabrication facilities and testing instruments essential for manufacturing and evaluating our specimens. We are particularly thankful to Mr. Michael Jiunn Jye Chung, the laboratory technician, for his invaluable assistance in facilitating our experiments within the laboratory.

Funding:

National Additive Manufacturing Innovation Cluster grant 2017015) (JYHF)

UCLA Robert Benson Estate Fund grant R47441-AZ (CMH)

Author contributions:

Conceptualization: CMH, JYHF

Methodology: CMH, JYHF, LY, JHK

Investigation, data acquisition, analysis, and interpretation: LY, JHK, CMH, JYHF, AK

Funding acquisition: JYHF, CMH

Project administration: JYHF, LY

Supervision: JYHF, CMH

Writing – original draft: CMH, LY

Writing – review & editing: LY, AK, CMH

Competing interests:

Related Patent

LY, JHK, CMH, and JYHF are co-inventors of the pending patent “Optimizing Process Parameters in Additive Manufacturing” (WO 2021/225529 A1).

Conflict of Interest

The authors declare that they have no other known competing financial interests or personal relationships that could have influenced the work reported in this paper.

Data and materials availability:

All the data used for this manuscript are available in the text and supplementary materials. Additional supplementary data are available upon request from Dr. Lina Yan at Linayan46@outlook.com.

References

1. Science, Special issue on complex systems. *Science* **275** (1997)
2. Science, Special issue on complex systems. *Science* **325** (2009)
3. National Research Council, Division on Engineering and Physical Sciences, Board on Physics and Astronomy, Physics Survey Overview Committee, *Physics in a New Era: An Overview, Chapter 2. Complex Systems* (The National Academies Press, Washington D.C., 2001).
4. Y. Holovatch, R. Kenna, S. Thurner, Complex systems: physics beyond physics. *Eur. J. Phys.* **38**, 23002 (2017), doi:10.1088/1361-6404/aa5a87.
5. Y. I. Wolf, M. I. Katsnelson, E. V. Koonin, Physical foundations of biological complexity. *Proceedings of the National Academy of Sciences of the United States of America*. **115**, E8678-E8687 (2018), doi:10.1073/pnas.1807890115.
6. J.-M. Lehn, Toward complex matter: supramolecular chemistry and self-organization. *Proceedings of the National Academy of Sciences of the United States of America*. **99**, 4763–4768 (2002), doi:10.1073/pnas.072065599.
7. T. M. Freeberg, R. I. M. Dunbar, T. J. Ord, Social complexity as a proximate and ultimate factor in communicative complexity. *Philosophical transactions of the Royal Society of London. Series B, Biological sciences*. **367**, 1785–1801 (2012), doi:10.1098/rstb.2011.0213.
8. J. Kwapien, S. Drożdż, Physical approach to complex systems. *Physics Reports*. **515**, 115–226 (2012), doi:10.1016/j.physrep.2012.01.007.
9. J. M. Ottino, Complex systems. *AIChE Journal*. **49**, 292–299 (2003), doi:10.1002/aic.690490202.
10. R. Gallagher, T. Appenzeller, Beyond Reductionism. *Science*. **284**, 79 (1999), doi:10.1126/science.284.5411.79.
11. M. I. Kaiser, The limits of reductionism in the life sciences. *History and philosophy of the life sciences*. **33**, 453–476 (2011).
12. M. H. V. van Regenmortel, Reductionism and complexity in molecular biology. Scientists now have the tools to unravel biological and overcome the limitations of reductionism. *EMBO reports*. **5**, 1016–1020 (2004), doi:10.1038/sj.embor.7400284.
13. F. Mazzocchi, Complexity in biology. Exceeding the limits of reductionism and determinism using complexity theory. *EMBO reports*. **9**, 10–14 (2008), doi:10.1038/sj.embor.7401147.
14. E. Ising, Beitrag zur Theorie des Ferromagnetismus. *Z. Physik*. **31**, 253–258 (1925), doi:10.1007/BF02980577.
15. C. N. Yang, The Spontaneous Magnetization of a Two-Dimensional Ising Model. *Physical Review*. **85**, 808–816 (1952), doi:10.1103/PhysRev.85.808.
16. G. Parisi, Number of Order Parameters for Spin-Glasses, *Physical Review Letters*. **43**, 1754–1756 (1979), doi:10.1103/PhysRevLett.43.1754
17. E. Schneidman, M. J. Berry, R. Segev, W. Bialek, Weak pairwise correlations imply strongly correlated network states in a neural population. *Nature*. **440**, 1007–1012 (2006), doi:10.1038/nature04701.

18. G. E. P. Box, K. B. Wilson, “On the Experimental Attainment of Optimum Conditions”, *Journal of the Royal Statistical Society: Series B, (Methodological)*, **13** (1) 1-38 (1951), doi.org/10.1111/j.2517-6161.1951.tb00067.x.
19. J. Pearl, *Causality: Models, reasoning, and inference, Reviewed by Leland Gerson Neuberger, Econometric Theory* (Cambridge University Press, Cambridge U.K., New York, 2003).
20. M. Mitchell, Complex systems: Network thinking. *Artificial Intelligence*. **170**, 1194–1212 (2006), doi:10.1016/j.artint.2006.10.002.
21. A.L. Barabási, Z. N. Oltvai, Network biology: understanding the cell’s functional organization. *Nature reviews. Genetics*. **5**, 101–113 (2004), doi:10.1038/nrg1272.
22. R. Aiyappa, A. Flammini, Y.Y. Ahn, Emergence of simple and complex contagion dynamics from weighted belief networks. *Science advances*. **10**, eadh4439 (2024), doi:10.1126/sciadv.adh4439.
23. I. Al-Shyoukh, F. Yu, J. Feng, K. Yan, S. Dubinett, C.M. Ho, J.S. Shamma, R. Sun, Systematic quantitative characterization of cellular responses induced by multiple signals. *BMC systems biology*. **5**, 88 (2011), doi:10.1186/1752-0509-5-88.
24. P. K. Wong, F. Yu, A. Shahangian, G. Cheng, R. Sun, C. M. Ho, Closed-loop control of cellular functions using combinatory drugs guided by a stochastic search algorithm. *Proceedings of the National Academy of Sciences of the United States of America*. **105**, 5105–5110 (2008), doi:10.1073/pnas.0800823105.
25. D. Ho, C. M. Ho, System control-mediated drug delivery towards complex systems via nanodiamond carriers. *International Journal of Smart and Nano Materials*. **1**, 69–81 (2010), doi:10.1080/19475411003619736.
26. H. Tsutsui, B. Valamehr, A. Hindoyan, R. Qiao, X. Ding, S. Guo, O. N. Witte, X. Liu, C. M. Ho, H. Wu, An optimized small molecule inhibitor cocktail supports long-term maintenance of human embryonic stem cells. *Nat Commun*. **2**, 167 (2011), doi:10.1038/ncomms1165.
27. A. Weiss, X. Ding, J. R. van Beijnum, L. Wong, T. J. Wong, R. H. Berndsen, O. Dormond, M. Dallinga, L. Shen, R. O. Schlingemann, R. Pili, C. M. Ho, P. J. Dyson, H. van den Bergh, A. W. Griffioen, P. Nowak-Sliwinska, Rapid optimization of drug combinations for the optimal angiostatic treatment of cancer. *Angiogenesis*. **18**, 233–244 (2015), doi:10.1007/s10456-015-9462-9.
28. A. Weiss, R. H. Berndsen, X. Ding, C. M. Ho, P. J. Dyson, H. van den Bergh, A. W. Griffioen, P. Nowak-Sliwinska, A streamlined search technology for identification of synergistic drug combinations. *Scientific reports*. **5**, 14508 (2015), doi:10.1038/srep14508.
29. A. Silva, B. Y. Lee, D. L. Clemens, T. Kee, X. Ding, C. M. Ho, M. A. Horwitz, Output-driven feedback system control platform optimizes combinatorial therapy of tuberculosis using a macrophage cell culture model. *Proceedings of the National Academy of Sciences of the United States of America*. **113**, E2172-9 (2016), doi:10.1073/pnas.1600812113.
30. X. Ding, W. Liu, A. Weiss, Y. Li, I. Wong, A. W. Griffioen, H. van den Bergh, H. Xu, P. Nowak-Sliwinska, C. M. Ho, Discovery of a low order drug-cell response surface for applications in personalized medicine. *Physical biology*. **11**, 65003 (2014), doi:10.1088/1478-3975/11/6/065003.
31. M. B. M. A. Rashid, T. B. Toh, L. Hooi, A. Silva, Y. Zhang, P. F. Tan, A. L. Teh, N. Karnani, S. Jha, C. M. Ho, W. J. Chng, D. Ho, E. K. H. Chow, Optimizing drug combinations against multiple myeloma using a quadratic phenotypic optimization platform (QPOP). *Sci. Transl. Med*. **10** (2018), doi:10.1126/scitranslmed.aan0941.
32. X. Ding, V. H. S. Chang, Y. Li, X. Li, H. Xu, C. M. Ho, D. Ho, Y. Yen, Harnessing an Artificial Intelligence Platform to Dynamically Individualize Combination Therapy for

- Treating Colorectal Carcinoma in a Rat Model. *Adv. Therap.* **3**, 1900127 (2020), doi:10.1002/adtp.201900127.
33. B. Y. Lee, D. L. Clemens, A. Silva, B. J. Dillon, S. Masleša-Galić, S. Nava, X. Ding, C. M. Ho, M. A. Horwitz, Drug regimens identified and optimized by output-driven platform markedly reduce tuberculosis treatment time. *Nat. Commun.* **8**, 14183 (2017), doi:10.1038/ncomms14183.
 34. A. Zarrinpar, D. K. Lee, A. Silva, N. Datta, T. Kee, C. Eriksen, K. Weigle, V. Agopian, F. Kaldas, D. Farmer, S. E. Wang, R. Busuttill, C. M. Ho, D. Ho, Individualizing liver transplant immunosuppression using a phenotypic personalized medicine platform. *Sci. Transl. Med.* **8**, 333ra49 (2016), doi:10.1126/scitranslmed.aac5954.
 35. A. J. Pantuck, D. K. Lee, T. Kee, P. Wang, S. Lakhotia, M. H. Silverman, C. Mathis, A. Drakaki, A. S. Belldegrun, C. M. Ho, D. Ho, Modulating BET Bromodomain Inhibitor ZEN-3694 and Enzalutamide Combination Dosing in a Metastatic Prostate Cancer Patient Using CURATE.AI, an Artificial Intelligence Platform. *Adv. Therap.* **1**, 1800104 (2018), doi:10.1002/adtp.201800104.
 36. Y. Shen, T. Liu, J. Chen, X. Li, L. Liu, J. Shen, J. Wang, R. Zhang, M. Sun, Z. Wang, W. Song, T. Qi, Y. Tang, X. Meng, L. Zhang, D. Ho, Dean; C. M. Ho, X. Ding, H. Z. Lu, Harnessing Artificial Intelligence to Optimize Long-Term Maintenance Dosing for Antiretroviral-Naive Adults with HIV-1 Infection. *Adv. Therap.* **3** (2020), doi:10.1002/adtp.201900114.
 37. T. Kee, W. Chee; A. Blasiak, P. Wang, J. K. Chong, J. Chen, B. T. T. Yeo, D. Ho, C. L. Asplund, Harnessing CURATE.AI as a Digital Therapeutics Platform by Identifying Identifying N-of-1 Learning Trajectory Profiles. *Adv. Therap.* **2** (2019), doi:10.1002/adtp.201900023.
 38. K. D. Miller, L. Nogueira, T. Devasia, A. B. Mariotto, K. R. Yabroff, A. Jemal, J. Kramer, R. L. Siegel, Cancer treatment and survivorship statistics, 2022. *CA: a cancer journal for clinicians.* **72**, 409–436 (2022), doi:10.3322/caac.21731.
 39. E. B. Maldonado, S. Parsons, E. Y. Chen, A. Haslam, V. Prasad, Estimation of US patients with cancer who may respond to cytotoxic chemotherapy. *Future science OA.* **6**, FSO600 (2020), doi:10.2144/fsoa-2020-0024.
 40. D. Ho, S. R. Quake, E. R. B. McCabe, W. J. Chng, E. K. Chow, X. Ding, B. D. Gelb, G. S. Ginsburg, J. Hassenstab, C. M. Ho, W. C. Mobley, G. P. Nolan, S. T. Rosen, P. Tan, Y. Yen, A. Zarrinpar, Enabling Technologies for Personalized and Precision Medicine. *Trends in biotechnology.* **38**, 497–518 (2020), doi:10.1016/j.tibtech.2019.12.021.
 41. Y. M. Wang, T. Voisin, J. T. McKeown, J. Ye, N. P. Calta, Z. Li, Z. Zeng, Y. Zhang, W. Chen, T. T. Roehling, R. T. Ott, M. K. Santala, P. J. Depond, M. J. Matthews, A. V. Hamza, T. Zhu, Additively manufactured hierarchical stainless steels with high strength and ductility. *Nat. Mater.* **17**, 63–71 (2018), doi:10.1038/nmat5021.
 42. C. Qiu, M. A. Kindi, A. S. Aladawi, I. A. Hatmi, A comprehensive study on microstructure and tensile behaviour of a selectively laser melted stainless steel. *Scientific reports.* **8**, 7785 (2018), doi:10.1038/s41598-018-26136-7.
 43. W. J. Boettinger, S. R. Coriell, A. L. Greer, A. Karma, W. Kurz, M. Rappaz, R. Trivedi, Solidification microstructures: recent developments, future directions. *Acta Materialia.* **48**, 43–70 (2000), doi:10.1016/S1359-6454(99)00287-6.
 44. O. Shuleshova, W. Löser, D. Holland-Moritz, D. M. Herlach, J. Eckert, Solidification and melting of high temperature materials: in situ observations by synchrotron radiation. *J Mater Sci.* **47**, 4497–4513 (2012), doi:10.1007/s10853-011-6184-2.

45. E. M. Sefene, State-of-the-art of selective laser melting process: A comprehensive review. *Journal of Manufacturing Systems*. **63**, 250–274 (2022), doi:10.1016/j.jmsy.2022.04.002.
46. Y. Zhang, G. S. Hong, D. Ye, K. Zhu, J. Y. Fuh, Extraction and evaluation of melt pool, plume and spatter information for powder-bed fusion AM process monitoring. *Materials & Design*. **156**, 458–469 (2018), doi:10.1016/j.matdes.2018.07.002.
47. C. Y. Yap, C. K. Chua, Z. L. Dong, Z. H. Liu, D. Q. Zhang, L. E. Loh, S. L. Sing, Review of selective laser melting: Materials and applications. *Applied Physics Reviews*. **2** (2015), doi:10.1063/1.4935926.
48. ASM International, Properties and Selection: Irons, Steels, and High-Performance Alloys. ASM Handbook, *ASM International*. **1** (1990).
49. W. E. King, A. T. Anderson, R. M. Ferencz, N. E. Hodge, C. Kamath, S. A. Khairallah, Laser powder bed fusion additive manufacturing of metals: physics, computational, and materials challenges. *Applied Physics Reviews*. **2**(4), 041304 (2015).
50. T. DebRoy, H. L. Wei, J. S. Zuback, T. Mukherjee, J. W. Elmer, J. O. Milewski, A. M. Beese, A. Wilson-Heid, W. Zhang, Additive manufacturing of metallic components – Process, structure and properties. *Progress in Materials Science*. **92**, 112-224 (2018).
51. O. Shuleshova, W. Löser, D. Holland-Moritz, D. M. Herlach, J. Eckert, Solidification and melting of high temperature materials: in situ observations by synchrotron radiation. *J Mater Sci*. **47**, 4497–4513 (2012), doi:10.1007/s10853-011-6184-2.
52. H. Tang, H. Huang, C. Liu, Z. Liu, W. Yan, Multi-Scale modelling of structure-property relationship in additively manufactured metallic materials. *International Journal of Mechanical Sciences*. **194**, 106185 (2021).
53. C. Zhao, K. Fezzaa, R. W. Cunningham, H. Wen, F. Carlo, L. Chen, A. D. Rollett, T. Sun, Real-time monitoring of laser powder bed fusion process using high-speed X-ray imaging and diffraction. *Scientific reports*. **7**, 3602 (2017), doi:10.1038/s41598-017-03761-2.

This list of reference is cited only in the supplementary materials:

54. B. K. Hayes, E. Heit, H. Swendsen, Inductive reasoning. *Wiley interdisciplinary reviews. Cognitive science*. **1**, 278–292 (2010), doi:10.1002/wcs.44.
55. A. Blasiak, J. J. Lim, S. G. K. Seah, T. Kee, A. Remus, H. Chye, P.S. Wong, L. Hooi, A. T. L. Truong, N. Le, C. E. Z. Chan, R. Desai, X. Ding, B.J. Hanson, E.K. Chow, D. Ho, IDentif.AI: Rapidly optimizing combination therapy design against severe Acute Respiratory Syndrome Coronavirus 2 (SARS-Cov-2) with digital drug development. *Bioengineering & Translational Medicine*. **6**, (2020), doi: 10.1002/btm2.10196.
56. ASTM, *E9-09 (2018) Standard Test Methods of Compression Testing of Metallic Materials at Room Temperature* (ASTM International, West Conshohocken, PA).
57. ASTM, *E03-11 (2017) Guide for Preparation of Metallographic Specimens* (ASTM International, West Conshohocken, PA).
58. ASTM, *E407-07 (2015) Practice for Microetching Metals and Alloys* (ASTM International, West Conshohocken, PA).
59. T. de Terris, O. Andreau, P. Peyre, F. Adamski, I. Koutiri, C. Gorny, C. Dupuy, Optimization and comparison of porosity rate measurement methods of Selective Laser Melted metallic parts. *Additive Manufacturing*. **28**, 802–813 (2019), doi:10.1016/j.addma.2019.05.035.
60. S. Bai, N. Perevoshchikova, Y. Sha, X. Wu, The Effects of Selective Laser Melting Process Parameters on Relative Density of the AlSi10Mg Parts and Suitable Procedures of the Archimedes Method. *Applied Sciences*. **9**, 583 (2019), doi:10.3390/app9030583.

61. O. Lopez-Botello, U. Martinez-Hernandez, J. Ramírez, C. Pinna, K. Mumtaz, Two-dimensional simulation of grain structure growth within selective laser melted AA-2024. *Materials & Design*. **113**, 369–376 (2017), doi:10.1016/j.matdes.2016.10.031.
62. S. Lee, J. Peng, D. Shin, Y. S. Choi, Data analytics approach for melt-pool geometries in metal additive manufacturing. *Science and Technology of Advanced Materials*. **20**, 972–978 (2019), doi:10.1080/14686996.2019.1671140.
63. L. E. Criales, Y. M. Arisoy, B. Lane, S. Moylan, A. Donmez, T. Özel, Predictive modeling and optimization of multi-track processing for laser powder bed fusion of nickel alloy 625. *Additive Manufacturing*. **13** (2017), doi:10.1016/j.addma.2016.11.004.
64. Y. Li, Y. Ge, J. Lei, W. Bai, Mechanical Properties and Constitutive Model of Selective Laser Melting 316L Stainless Steel at Different Scanning Speeds. *Advances in Materials Science and Engineering*. **2022**, 1–13 (2022), doi:10.1155/2022/2905843.
65. M. Güden, S. Enser, M. Bayhan, A. Taşdemirci, H. Yavaş, The strain rate sensitive flow stresses and constitutive equations of a selective-laser-melt and an annealed-rolled 316L stainless steel: A comparative study. *Materials Science and Engineering: A*. **838**, 142743 (2022), doi:10.1016/j.msea.2022.142743.
66. J. Lei, Y. Ge, T. Liu, Z. Wei, Effects of Heat Treatment on the Microstructure and Mechanical Properties of Selective Laser Melting 316L Stainless Steel. *Shock and Vibration*. **2021**, 1–12 (2021), doi:10.1155/2021/6547213.
67. X. Li, M. Ghasri-Khouzani, A.-A. Bogno, J. Liu, H. Henein, Z. Chen, A.J. Qureshi, Investigation of Compressive and Tensile Behavior of Stainless Steel/Dissolvable Aluminum Bimetallic Composites by Finite Element Modeling and Digital Image Correlation. *Materials (Basel, Switzerland)*. **14** (2021), doi:10.3390/ma14133654.
68. M. Ghasri-Khouzani, X. Li, A.A. Bogno, Z. Chen, J. Liu, H. Henein, A.J. Qureshi, Fabrication of aluminum/stainless steel bimetallic composites through a combination of additive manufacturing and vacuum-assisted melt infiltration casting. *Journal of Manufacturing Processes*. **69**, 320–330 (2021), doi:10.1016/j.jmapro.2021.07.047.
69. B. Diepold, S. Neumeier, A. Meermeier, H.W. Höppel, T. Sebal, M. Göken, Temperature-Dependent Dynamic Strain Aging in Selective Laser Melted 316L. *Adv Eng Mater*. **23**, 2001501 (2021), doi:10.1002/adem.202001501.
70. Q. Chao, S. Thomas, N. Birbilis, P. Cizek, P.D. Hodgson, D. Fabijanic, The effect of post-processing heat treatment on the microstructure, residual stress and mechanical properties of selective laser melted 316L stainless steel. *Materials Science and Engineering: A*. **821**, 141611 (2021), doi:10.1016/j.msea.2021.141611.
71. J. Kluczyński, L. Śnieżek, K. Grzelak, J. Janiszewski, P. Płatek, J. Torzewski, I. Szachogłuchowicz, K. Gocman, Influence of Selective Laser Melting Technological Parameters on the Mechanical Properties of Additively Manufactured Elements Using 316L Austenitic Steel. *Materials (Basel, Switzerland)*. **13** (2020), doi:10.3390/ma13061449.
72. J. Liu, Y. Song, C. Chen, X. Wang, H. Li, C. Zhou, J. Wang, K. Guo, J. Sun, Effect of scanning speed on the microstructure and mechanical behavior of 316L stainless steel fabricated by selective laser melting. *Materials & Design*. **186**, 108355 (2020), doi:10.1016/j.matdes.2019.108355.
73. A. Röttger, J. Boes, W. Theisen, M. Thiele, C. Esen, A. Edelmann, R. Hellmann, Microstructure and mechanical properties of 316L austenitic stainless steel processed by different SLM devices. *Int J Adv Manuf Technol*. **108**, 769–783 (2020), doi:10.1007/s00170-020-05371-1.

74. Q. Portella, M. Chemkhi, D. Retraint, Influence of Surface Mechanical Attrition Treatment (SMAT) post-treatment on microstructural, mechanical and tensile behaviour of additive manufactured AISI 316L. *Materials Characterization*. **167**, 110463 (2020), doi:10.1016/j.matchar.2020.110463.
75. G. S. Ham, S. H. Park, K. A. Lee, Room and Elevated Temperature Compressive Deformation Behavior of AISI 316L Alloy Fabricated by Selective Laser Melting Process. *Korean J. Met. Mater.* **57**, 295–303 (2019), doi:10.3365/KJMM.2019.57.5.295.
76. T. Kurzynowski, K. Gruber, W. Stopyra, B. Kuźnicka, E. Chlebus, Correlation between process parameters, microstructure and properties of 316 L stainless steel processed by selective laser melting. *Materials Science and Engineering: A*. **718**, 64–73 (2018), doi:10.1016/j.msea.2018.01.103.
77. W. Chen, G. Yin, Z. Feng, X. Liao, Effect of Powder Feedstock on Microstructure and Mechanical Properties of the 316L Stainless Steel Fabricated by Selective Laser Melting. *Metals*. **8**, 729 (1–12) (2018), doi:10.3390/met8090729.
78. L. Hitzler, J. Hirsch, B. Heine, M. Merkel, W. Hall, A. Öchsner, On the Anisotropic Mechanical Properties of Selective Laser-Melted Stainless Steel. *Materials*. **10** (2017), doi:10.3390/ma10101136.
79. J. Suryawanshi, K. G. Prashanth, U. Ramamurty, Mechanical behavior of selective laser melted 316L stainless steel. *Materials Science and Engineering: A*. **696**, 113–121 (2017), doi:10.1016/j.msea.2017.04.058.
80. E. Liverani, S. Toschi, L. Ceschini, A. Fortunato, Effect of selective laser melting (SLM) process parameters on microstructure and mechanical properties of 316L austenitic stainless steel. *Journal of Materials Processing Technology*. **249**, 255–263 (2017), doi:10.1016/j.jmatprotec.2017.05.042.
81. Y. Zhong, L. Liu, S. Wikman, D. Cui, Z. Shen, Intragranular cellular segregation network structure strengthening 316L stainless steel prepared by selective laser melting. *Journal of Nuclear Materials*. **470**, 170–178 (2016), doi:10.1016/j.jnucmat.2015.12.034.

Supplementary Materials for
**A ubiquitous transfer function links interacting elements to emerging
property of complex systems**

Lina Yan^{1†}, Jeffrey Huy Khong^{2†}, Aleksandar Kostadinov³, Jerry Ying Hsi Fuh^{1*}, Chih-Ming
Ho^{1,4*}

Corresponding author: c.ho1945@gmail.com

The PDF file includes:

Supplementary Text
Materials and Methods
Figs. S1 to S2
Tables S1 to S5

1. Model Equations and Network Analyses of Complex Systems

1.1 Model Equations

Studies of complex systems frequently rely on model-based equations to link interacting components with emergent properties. Among the many model-based equations for complex systems, we will discuss two models that utilize polynomial-type equations at here.

Applying these model equations requires strict adherence to the assumptions made during their derivation and compliance with fundamental physical laws, particularly the principle of causality.

1.1.1 Ising Model

Many second-order polynomial equations model various natural phenomena, such as the Ising mode (14). This physical model describes discrete (+1 or -1) magnetic dipoles in a lattice. The spin configuration, σ , of a lattice can change through interactions with other lattices. The physical model equation is given in Equation-S1. Here, $H(\sigma)$ represents the energy of the system of magnetic dipoles. The first-order terms, $-\sum_j h_j \sigma_j$ represent the effect of external magnetic fields on the system. The second-order terms, $-\sum_{i,j} J_{ij} \sigma_i \sigma_j$, represent the interactions among different lattices

$$H(\sigma) = -\sum_j h_j \sigma_j - \sum_{i,j} J_{ij} \sigma_i \sigma_j$$

..... (Equation-S1)

The Ising model has been applied to various fields, including magnetism (15), and spin glasses (16). Since a neuron at a given time can be either “active” or “inactive”, the statistical activities of neurons can also be modelled by the Ising function (17).

1.1.2 Response Surface Method (RMS) equation

Response Surface Method (RMS) equation (18) is derived by expanding a function, η , into a polynomial series (54).

$$\eta = \beta_0 + \beta_1 \chi_1 + \beta_2 \chi_2 + \dots + \beta_{11} \chi_1^2 + \dots + \beta_{12} \chi_1 \chi_2 + \dots + \beta_{111} \chi_1^3 + \dots$$

..... (Equation-S2)

In the above equation, the function, η , is the cause, while the terms on the right-hand side represent consequences. In the realm of complex systems, the emergent property assumes the role of consequence, while the interactions among elements serve as the causes. It's worth noting that the RMS equation deviates from the principles of causality (19).

Furthermore, the RSM equation was postulated based on three assumptions:

1. As the function, η , was mathematically expanded into a polynomial series, it was presumed that the coefficients β_i , β_{ii} , and β_{ij} remain constant. Should these coefficients deviate from constants, a further expansion into series of their own parameters would be necessary.
2. The third and high order terms were assumed to be negligible.
3. It was posited that the optimal value resides at the stationary point. This assertion holds true only if the response surface exhibits an elliptic paraboloid shape. Conversely, if the response

surface takes the form of a hyperbolic paraboloid, the optimal value will manifest at the boundary.

In chemical reactions, the chemical energy of a molecule post-reaction remains constant, and the reaction time is exceedingly brief, thereby allowing the coefficients of RSM equation to hold approximately constant, although they still violate the causality law. On the other hand, in biological and physical complex systems, the first assumption of constant coefficients is untenable. Moreover, it's common for the response surface to be a hyperbolic paraboloid, thus nullifying the validity of the third assumption. Given the considerations outlined above, except for applications in chemistry, the trial-and-error method remains prevalent in both research communities and industries.

1.2 Networks Analyses

Network analysis (20–22) represents a potent approach for investigating how self-organization unfolds. Significant strides have been achieved in mapping the intricate network structures found in biological, physical, chemical, and social complex systems. Current research frontiers are dedicated to delineating the functional and quantitative attributes of interaction nodes, as well as understanding how networks undergo reorganization at different stages within the hierarchical complex systems.

2. Complex System Response (CSR) Function

2.1 A Precursor of CSR Platform - Feedback System Control (FSC) Platform

Combinatorial treatments are widely used in managing nearly all diseases, yet optimizing dosages remains a significant challenge. With L doses for each of P drugs, the search space includes L^P drug-dose combinations, making it an arduous task to find an optimal regimen.

Game theory has played a crucial role in addressing this challenge through the Feedback System Control (FSC) scheme. FSC promises to identify the optimal regimen in fewer than 20 iterative loops, significantly reducing the computational burden compared to the exhaustive L^P searches. This breakthrough has been validated through numerous in vitro tests across various disease models (24–27).

2.2 AI Complex System Response (CSR) Function

By examining the experimental database of ATP production in a cancer cell line stimulated by a combinatorial regimen, the system response (an emerging property of the biological complex system) was revealed as a smooth response surface within the multi-dimensional drug-dose space. Regression analysis of this smooth response surface can be represented by a nonlinear function (23). The discovery of a second-order nonlinear function (Function-S1) has been generalized through several dozen in vitro, animal, and clinical tests (23, 28–37). The R^2 values of the raw data, without additional iterative data, were found to be close to unity.

$$E = x_0 + \sum_{i=1}^P x_i c_i + \sum_{i=1}^P x_{ii} c_i^2 + \sum_{i=1}^{P-1} \sum_{j=i+1}^P x_{ij} c_i c_j$$

..... (Function-S1)

Through a detailed examination of the properties of coefficients as outlined in references (32) and (33), the generalized form of the CSR function is presented as Function 1 in the main text. The coefficients in Function-S1 are not constants; instead, they are function of time, unknown parameters, and other independent variables. For example, x_i is a function of c_k , and $k \neq i$.

The Function-1 comprises $(P^2 + 3P + 2)/2$ coefficients. By conducting a small number of $(P^2 + 3P + 2)/2 < L^P$ calibration tests on the specific patient's physiological system, we can solve for these coefficients and discern the customized optimal personalized regimen (37–40).

In big-data deep learning, using large number of patients to train a multi-layer neural network. The population-based response pattern will not be simple smooth surface and cannot be presented by a second order function. The outcome from population-averaged approach will not fit for a specific patient.

Many names have been associated with the CSR platform. In the early stages of developing the transfer function, Feedback System Control (FSC), flexible or streamlined Feedback System Control (s-FSC) were utilized (26–29). Later, the Phenotypic Response Surface (PRS or PRS) function replaced FSC or s-FSC for applications in biological complex systems (34, 36). Other research groups used CURATE.AI (37), QPOP (31), and IDentif.AI (55). Eventually, the CSR function was adopted after the discovery that Function-1 could serve as a general transfer function for physical complex systems.

2.3 Protocol of Implementing CSR Function

The conventional approach to identifying the optimal combinatorial drug involves searching through a vast parameter-level space, L^P , formed by L dosing levels for each drug in a pool of P drugs. However, with the CSR function, only a small number, $(P^2 + 3P + 2)/2$ (much less than L^P , of tests are required to identify the global optimum across the entire range of parameter-level combinations.

The protocol is as follows:

1. Based on the CSR function (Function-1), determine the number of necessary tests, which is $(P^2 + 3P + 2)/2$.
2. Define the minimum and maximum levels for each parameter.
3. Strategically distribute the $(P^2 + 3P + 2)/2$ parameter-level (e.g., drug-dose) combinations over the P-dimensional parameter-level space using Orthogonal Array Composite Designs (OACD) (29,30).
4. Experimentally measure the $(P^2 + 3P + 2)/2$ system outcomes.
5. Solve for the $(P^2 + 3P + 2)/2$ coefficients of the CSR function.
6. Identify the global optimal system outcome and the corresponding best parameter-level combinations.

For personalized therapy, dynamic dosing is essential:

1. Sequentially apply the OACD-designed parameter-level pairs over time.
2. At the end of the $(P^2 + 3P + 2)/2$ tests, determine the optimal dose for the next dosing.
3. Continue the dynamic optimization using the moving-window method.

3. Materials and Methods

3.1 Sample Preparation

Stainless steel 316L specimens were produced using the Selective Laser Melting (SLM) technique. The specimens, conforming to the ASTM E9 standard (56), were designed with a cylindrical geometry, with a diameter and height of 5 mm each. The fabrication was performed on an EoS M290 SLM system (EoS, Germany), utilizing recycled 316L stainless steel powder with a particle size distribution ranging from 50 to 80 μm (Retsch GmbH, Germany).

The fabrication parameters were systematically varied in this investigation, including laser power (P) ranging from 80 to 190 W, scanning velocity (V) from 100 to 2500 mm/s, and powder bed temperature (T) between 25 and 160 $^{\circ}\text{C}$. The default settings for the process included a hatch distance (h) of 0.09 mm, layer thickness (l) of 0.02 mm, and a laser spot size, equivalent to the focus diameter, of 0.08 mm. The oxygen level in the chamber was controlled to remain below 0.2% to minimize oxidation during the process. The scanning strategy employed a bi-directional pattern with a 67° rotation after each layer deposition to ensure uniform material distribution. The energy density (E), a critical parameter representing the laser energy per unit volume for powder melting, was calculated using the formula $E = P / (V \times h \times l)$, where P , V , h , and l correspond to laser power, scanning velocity, hatch distance, and layer thickness, respectively.

Following the SLM process, the specimens were detached from the build platform using wire cutting. To alleviate residual stresses, the specimens underwent furnace heating from ambient temperature to 400 $^{\circ}\text{C}$ over a period of one hour, followed by soaking at this temperature for 4 hours, and subsequently cooled to room temperature within the furnace.

3.2 Mechanical tests

The compressive tests were conducted using Instron 8848 (Instron, USA) following the ASTM E9 test protocol (56). An adjustable bearing block made of tungsten carbide was employed to evenly distribute the initial load. The compressive yield stress was recorded at the strain offset at 0.2%.

3.3 Area Density Function Measurement

The internal structure of samples was exposed in the XY and XZ (or YZ) planes which run perpendicular and parallel to the build direction (fig. S1). The surfaces were ground and polished to a mirror finish, followed by electrolytic etching using oxalic acid as per ASTM E3-11 and ASTM E407 standard (57, 58). The etching parameters included a voltage of approximately 6 V and a current of 0.35 A for a duration of 60 seconds. Optical microscopic images were taken on both planes using bright field Nikon eclipse LV 150 N (Nikon, Japan) at a magnification of 100 times for an area of approximately 1 mm by 1 mm (fig. S1).

The porosity present within the samples was quantitatively assessed by digital image analysis. Initially, images captured on both XY and XZ planes were processed to distinguish porous regions from the solid matrix based on pixel contrast. The percentage of the porous

region was calculated using ImageJ, an open-source image processing software developed by the National Institutes of Health, United States (<https://imagej.net/ij/index.html>).

The volumetric area fraction of density (VAFD) of each sample was estimated by a geometrical factor that accounts for the porosity in both the XY and XZ planes (59, 60). The formula applied was derived from the principle that the density of a sample can be inferred from the volume fraction of solid material present. The calculation was performed using the expression:

$$VAFD = [(1 - P_{XY}) \times (1 - P_{XZ})] / side_length$$

Where P_{XY} and P_{XZ} represent the porosity percentages measured on the respective planes, and the side length is 1mm for the images used in analysis.

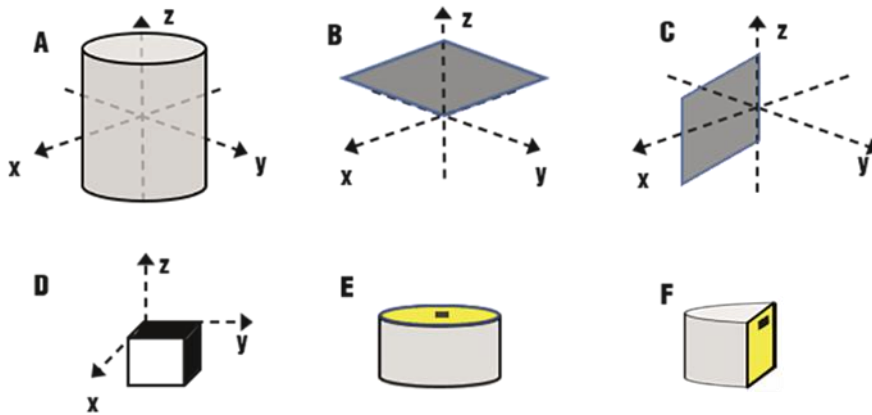


fig. S1. Schematic demonstration of the cutting planes in the 3D system.

(A) The SLM fabricated specimen with coordinate system indicated, where z is the build direction. (B) and (C) indicate the exposed internal surfaces in the XY plane and XZ plane (or YZ plane) via wire cutting. (D) The exposed surfaces on the XY and XZ planes, the volume of this unit can be calculated by $Volume = (A_{XY} \times A_{XZ}) / unit_length$. (E) and (F) The yellow highlighted surfaces indicate the exposed plane after cutting, and the black areas indicate the microscopic imaging area. Notes: this is used for demonstration purpose, not representing the real scale of samples.

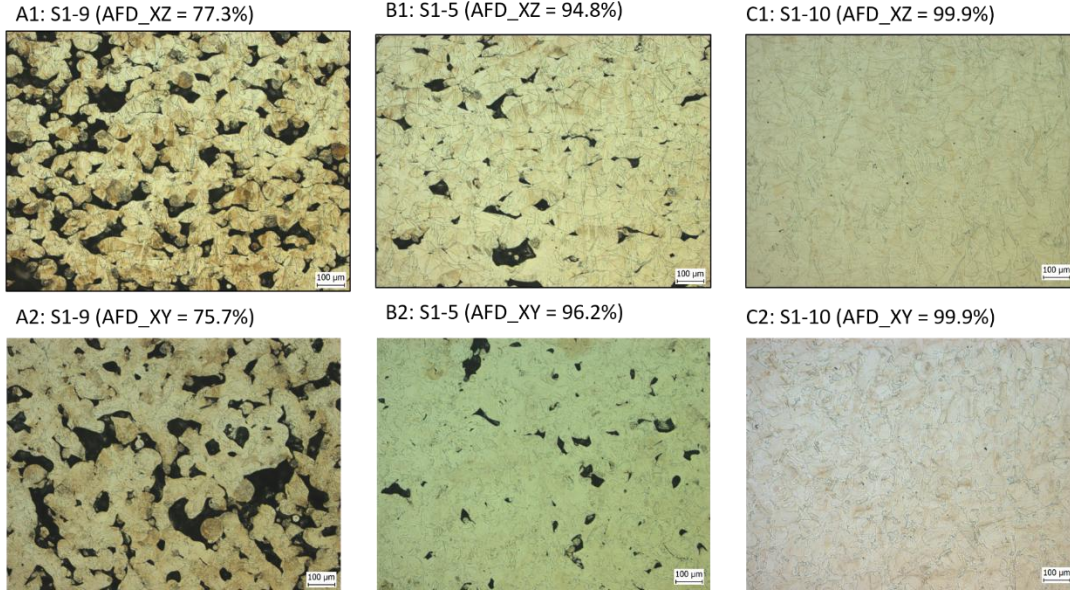


fig. S2. Demonstration of $VAFD$ from high porosity specimen S1-9 to S1-5 and full density S1-10.

$$VAFD = [(1 - P_{XY}) \times (1 - P_{XZ})] / side_length$$

(A) The microscopic images of XZ and XY plane for sample S1-9, the porosity was 77.3% and 75.7%, the calculated $VAFD$ is 58.5%. (B) The microscopic images of XZ and XY plane for sample S1-5, the porosity was 94.8% and 96.2%, the $VAFD$ is 91.2%. (C) The microscopic images of XZ and XY plane for sample S1-10, the porosity was 99.9% and 99.9%, the $VAFD$ is 99.8%.

3.4 Melt Pool Analysis

The melt pool boundary (MPB), also known as fusion line, is the interface that arises between the newly solidified material and the pre-existing solid substrate as a result of a single laser pass. In this investigation, the approach to melt pool analysis diverges from previous by employing a mass-analysis method (42, 61–63), which provides a comprehensive understanding of melt pool characteristics. The width (W) and depth (D) of melt pool boundaries were measured on the XZ plane images which provides a cross-sectional view of the melt pool (fig. S2-A) (42, 61–63). More than one hundred melt pool boundaries were quantitatively measured and analyzed, as depicted in fig. S2-B. The length of major and minor axis of fitted ellipses were summarized, and converted to the size of real melt pool boundaries based on the ratio of the scale bar on the image. Lastly, the average width and depth of melt pool obtained from more than 100 fittings were used to calculate the average volume of melt pool.

Refer to fig. S2-C, since the cross-section of the melt pool boundaries was simplified as a semi-ellipse, the area of the section can be estimated by $(\pi \times W \times D) / 4$. At a given *laser scanning speed* mm/s in unit time during one melting pass, the volume of a melt pool (VMP) can be estimated by $(\pi \times W \times D \times V) / 4$ mm³/sec (42, 61–63).

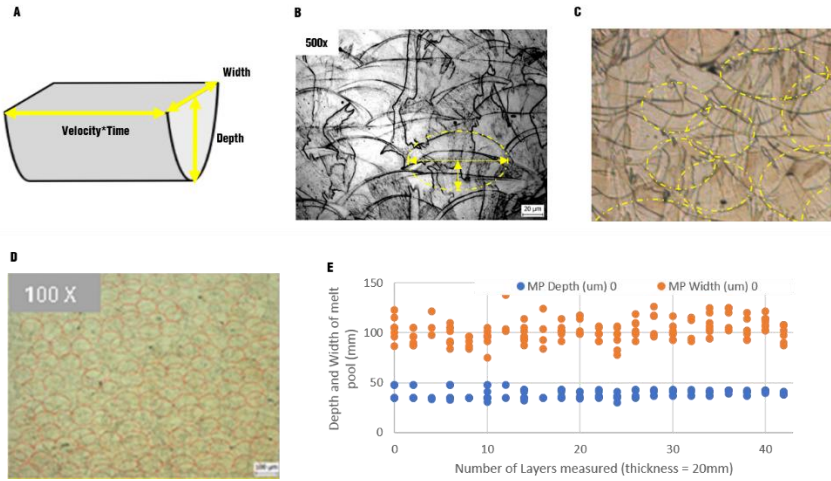


fig. S3. Measurement of melt pool depth and width.

(A) A schematic plot illustrates the volumetric properties of the melt pool. (B) An yellow elliptical fitting of a melt pool boundary is demonstrated on an image captured at 500 times magnification, the width and depth of melt pool can be estimated as the length of major axis and half of minor axis; (C) & (D) Section view and full view of all recognizable melt pool boundaries were fitted on a microscopic image taken at 100 times magnification, representing an area of $1 \text{ mm} \times 1 \text{ mm}$; (E) The average value of melt pool depth and width were summarized with respect to the number of printed layers (layer thickness of 20mm).

4. Tables of experimental data

Table S1. Summary of process parameters and compressive yield stress (CYS).

Of the 16 initial specimens (S1-1 to S1-16), five were excluded from final analyses due to processing issues. Specimens S1-2 and S1-6 featured an energy density of 22.2 J/mm³, which was insufficient for powder melting, resulting in specimens with cavities unsuitable for mechanical property analysis. Conversely, specimens S1-3, S1-7, and S1-11 exhibited high energy densities of 263.9 J/mm³ and 222.2 J/mm³, respectively, leading to over-melting and significant distortion. The remaining 11 specimens, with their process parameters and compressive yield stress, are detailed in this table.

Batch-1	Power P (W)	Velocity V(mm/s)	Temperature T (°C)	Energy density E (J/mm ³)	Compressive Yield Stress CYS (MPa)
S1-1	190	2000	160	52.8	437.1
S1-2	80	2000	160	22.2	-
S1-3	190	400	160	263.9	-
S1-4	80	400	160	111.1	534.2
S1-5	190	2000	25	52.8	413.1
S1-6	80	2000	25	22.2	-
S1-7	190	400	25	263.9	-
S1-8	80	400	25	111.1	534.1
S1-9	80	1400	70	31.7	243.1
S1-10	120	800	70	83.3	554.3
S1-11	160	400	115	222.2	-
S1-12	120	1400	160	47.6	302.6
S1-13	120	1400	25	47.6	361.3
S1-14	160	1400	115	63.5	474
S1-15	160	900	25	98.8	446.2
S1-16	120	2000	70	33.3	249.6

Table S2. The CSR Functions for process parameters and compressive yield stress (CYS).

Batch-1	CSR Function	R ²
(E, T)	$CYS = -7.54 \times 10 + 1.12 \times 10 \times E + 7.94 \times 10^{-1} \times T$ $-5.55 \times 10^{-2} \times E^2 - 3.59 \times 10^{-3} \times T^2 + 7.38 \times 10^{-4} \times E \times T$	0.898
(P, V, T)	$CYS = 2.2 \times 10^{-1} + 1.18 \times 10 \times P - 8.66 \times 10^{-1} \times V + 5.24 \times T$ $-4.78 \times 10^{-2} \times P^2 + 4.92 \times 10^{-5} \times V^2 - 2.01 \times 10^{-2} \times T^2$ $+3.55 \times 10^{-3} \times P \times V - 2.6 \times 10^{-2} \times P \times T + 1.64 \times 10^{-3} \times V \times T$	0.831

Table S3. The Maximum compressive yield stress at its optimal fabrication parameter-level calculated from CSR Functions.

E (J /mm ³)	T (oC)	P (W)	V (mm/s)	Optimal CYS (MPa)
102	121	94	500	545

Table S4. A summary of the reported SLM process parameters and the corresponding yield stresses of stainless steel 316L

References	Laser Power (W)	Scanning velocity (mm/s)	Powder Bed temperature (oC)	Energy Density (J/mm ³)	Compressive Yield Stress (MPa)	Tensile Yield Stress (MPa)
Li et al. 2022 (64)	180	650	-	55.4	584	-
Güden et al. 2022 (65)	370	900	-	120	~ 580	
Lei et al. 2021 (66)	200	1000	-	40	544	-
Li et al. 2021; Ghasri-Khouzani et al. 2021 (67,68)	195	1083	80	112.5	~ 520	~500
Diepold et al. 2021 (69)	-	-	-	-	~ 360	~370
Chao et al. 2021 (70)	175	730	200	66.6	-	418
Kluczyński et al. 2020 (71)	190	900	-	58.6	~ 550	554
Liu et al. 2020 (72)	215	1000	-	87.4	-	707
Röttger et al. 2020 (73)	136.1	928.1	80	36.7	-	503.1
Portella et al. 2020 (74)	150	400	150	93.8	-	527
Ham et al. 2019 (75)		-	-	-	536	-
Kurzynowski et al. 2018 (76)	100	220	-	81	-	517
Chen et al. 2018 (77)	200	2000	-	55.6	-	519
Hitzler et al. 2017 (78)	200	800	200	69.4	-	590
Suryawanshi et al. 2017 (79)	90	1000	-	20	-	536
Liverani et al. 2017 (80)	150	700	-	153.1	-	~520
Zhong et al. 2016 (81)	200	1000	-	40	-	487

Table S5. The coefficients of CRS function at the optimal and off-optimal CYS.
 (A) CYS = 545 MPa, E = 102 J/mm³, T = 121°C; (B) CYS = 488.34 MPa, E = 70 J/mm³, T = 121°C; (C) CYS = 395.21 MPa, E = 50 J/mm³, T = 121°C.

$CYS = -7.54 \times 10 + 1.12 \times 10 \times E + 7.94 \times 10^{-1} \times T - 5.55 \times 10^{-2} \times E^2 - 3.59 \times 10^{-3} \times T^2 + 7.38 \times 10^{-4} \times E \times T$								
CYS(MPa)	E(J/mm ³)	T(°C)	x ₀	x _E	x _T	x _{EE}	x _{TT}	x _{TE}
545	102	121	-3.86%	+58.6%	+4.92%	-29.5%	-2.69%	+0.47%
488	70	121	-5.85%	+61.0%	+7.46%	-21.1%	-4.08%	+0.49%
395	50	121	-8.12%	+60.5%	+10.4%	-14.9%	-5.66%	+0.48%

Table S-6: The calculated area fraction of density (VAFD) and volume of melt pool (VMP) are listed in this Table.

The volume of a melt pool (VMP) was estimated by $VMP = (\pi \times W \times D \times V) / 4$ mm³/sec, where W and D are the average width and depth of melt pool boundary, and V is the scanning velocity. The VMP varied from 0.938 mm³/s to 3.711 mm³/s. The averaged melt pool boundary width was 0.089 mm and close to the laser beam diameter of 0.080 mm. On average, the width was 11% larger than the laser diameter. The average melt pool depth was 0.034 mm, and the metal powder layer thickness for each print was 0.020 mm. Thus, the average melt pool depth was 70% times larger than metal powder layer thickness for each print.

Batch 1	Width W (mm)	Depth D (mm)	Velocity V (mm/s)	Volume of Melt pool VMP (mm ³ /s)	Volumetric Area Fraction of Density VAFD (%)
S1-1	0.0809	0.0292	2000	3.711	96.4
S1-4	0.0927	0.0322	400	0.938	99.8
S1-5	0.0762	0.0306	2000	3.663	91.2
S1-8	0.102	0.0383	400	1.227	99.6
S1-9	0.0661	0.0244	1400	1.773	58.5
S1-10	0.0911	0.0357	800	2.043	99.8
S1-12	0.0891	0.0352	1400	3.449	89.6
S1-13	0.0834	0.0314	1400	2.879	84.0
S1-14	0.075	0.0306	1400	2.523	90.2
S1-15	0.0845	0.0357	900	2.132	99.8
S1-16	0.0673	0.0253	2000	2.675	54.7